PCCP

Accepted Manuscript

ROYAL SOCIETY OF CHEMISTRY

www.rsc.org/pccp

Capacitive Charging and Desalination Dynamics of a Packed-Bed Reactor

Mengying Li, Howard H. Hu, and Haim H. Bau
Department of Mechanical Engineering and Applied Mechanics
University of Pennsylvania

Abstract

We study theoretically the charging and desalination dynamics of a packed-bed reactor comprising two percolating granular aggregates that form two porous electrodes. The two porous electrodes are separated with an ion-permeable, electrically insulating spacer, are confined between two long, parallel, current collecting plates, and are saturated with an electrolyte solution. The porous electrodes are ideally polarizable. The electrolyte is binary, and dilute. The electric double layers next to the pore surface are thin. We use volume-averaging (homogenization) theory for porous electrodes and the Gouy-Chapman-Stern model for the electric double layer. Both the cases of finite and infinite aggregate electric conductivities subjected to step changes in the collecting plates' potentials are considered. We determine the potential and concentration distributions and the charging time as functions of space, time, and reactor characteristics. Significantly, we find that the charging time depends only weakly on the solid matrix conductivity as long as the solid matrix conductivity is of comparable magnitude or greater than that of the electrolyte. Furthermore, there is an optimal, finite solid matrix conductivity for which the charging time is minimized.

Keywords: supercapacitor, energy storage, desalinator, capacitive deionization, Poisson-Nernst-Planck

1. Introduction

Inexpensive energy storage and recovery are critical for, among other things, improving the utilization and reliability of the electrical grid by decoupling power generation from fluctuating demand [1-3]; enabling continuous utilization of energy from fluctuating renewable energy sources such as solar and wind [3]; powering high-demand applications [4]; and recovering energy in hybrid and electrical vehicles [5]. Electrochemical Capacitors (ECs, also known as electric double-layer capacitors or supercapacitors) offer an attractive alternative to batteries as energy storage devices [6]. In contrast to traditional batteries, the ECs store energy in the electric double layer. Since the charge / discharge process is based on ion migration and does not involve electrochemical (Faradaic) reactions, ECs are uniquely suited for high power density applications and enjoy much greater life expectancy than batteries. An EC can operate millions of cycles without degradation, compared to about a thousand cycles of a typical battery. Conventional ECs suffer, however, from low energy storage density compared to that of batteries.

Generally, in energy converting devices, it is desirable to decouple the power producing unit from the energy storage unit. For example, in an internal combustion engine, the power is dictated by the size of the engine and the energy storage capacity is dictated by the fuel tank's volume. In contrast, the volume of traditional batteries and ECs dictate both power and energy capacities. To overcome this shortcoming, redox flow batteries were introduced in the 1960s [8, 9]. In a redox flow battery, an ion-selective membrane separates the redox couple. During operation, redox-active species flow from storage tanks, undergo oxidation or reduction when contacting the current collectors, and proceed to another set of storage tanks, thereby decoupling energy storage from power capacity. The energy storage capacity can be controlled by varying the volume of the storage tanks. The energy storage density of redox flow batteries is, however, limited by the redox species' solubility (~8M) to about 25Wh/kg.

To overcome the limitations of redox flow batteries, Chiang et al. [10-12] have proposed semi-solid flow Li batteries. Instead, of flowing the electrolyte, their battery employs "flowing electrodes," comprising slurries of colloidal particles, such as $LiCoO_2$ and $Li_4Ti_5O_{12}$, dispersed in suspensions of Ketjen (carbon black particles, ~35nm diameter) to form conductive "inks." The slurries are stored in reservoirs. To charge/discharge the system, the two suspensions, separated

with a Li-permeable membrane, circulate through the current collector. While in the collector, the colloids assemble into electrically conducting networks and operate as conventional Li-ion batteries. The semi-solid flow battery combines the high energy storage density of the Li-ion battery while decoupling the energy storage from the power generation capacity. As in the case of the redox flow batteries, the reservoirs can be filled with "charged" particles, reducing the excessive charging time of conventional batteries.

More recently, Presser et al [13] have recognized that the concept of "flowing electrodes" can also be adapted to electrochemical capacitors with benefits similar to the ones achieved with semi-solid flow batteries (Fig. 1). The electrochemical flow capacitors (EFC) are comprised of carbon microparticles suspended in an electrolyte solution. Carbon is the material of choice for the microparticles because it is porous with a large surface area, inert, inexpensive, environmentally-benign, and of low friction. When storing energy, two suspensions of uncharged particles flow from two storage tanks into the current collector, where the particles aggregate to form two percolated, electrically-conducting networks (Fig. 1). Each of the formed porous electrodes contacts a collector plate. As electrons flow from the collector plates to the particles, mobile counter-ions in the suspending solution migrate to the surfaces of the pores both inside and around the particles to form electric double layers. Subsequent to the charging process, the particles are re-suspended, while maintaining their electrical charges and their counter-ion envelopes, and flow into the charged-particles' storage tanks. In essence, each particle serves as a minute capacitor. The slurry can be discharged in a similar manner to recover the stored electrical energy. Interestingly, the idea of charging colloidal particles "on the fly" is not new, and has been previously implemented in waste remediation devices [14].

Since the EFCs absorb ions from solution in the electric double layers, they are also well-suited for water desalination. In contrast to the better known desalination methods, such as distillation, reverse and forward osmosis, and electrodialysis, that extract fresh water from the salt solution, capacitive deionization (CDI) removes salt ions from the solution, leaving fresher water behind. CDI is a robust, energy efficient, cost-effective technology for the desalination of brackish water with salt concentrations under 1% [23, 24]. Conventional CDIs operate in two discontinuous steps: an ion absorption (charging) step, wherein ions are transported from the brackish water into the electrical double layers engulfing the porous electrodes; followed by a

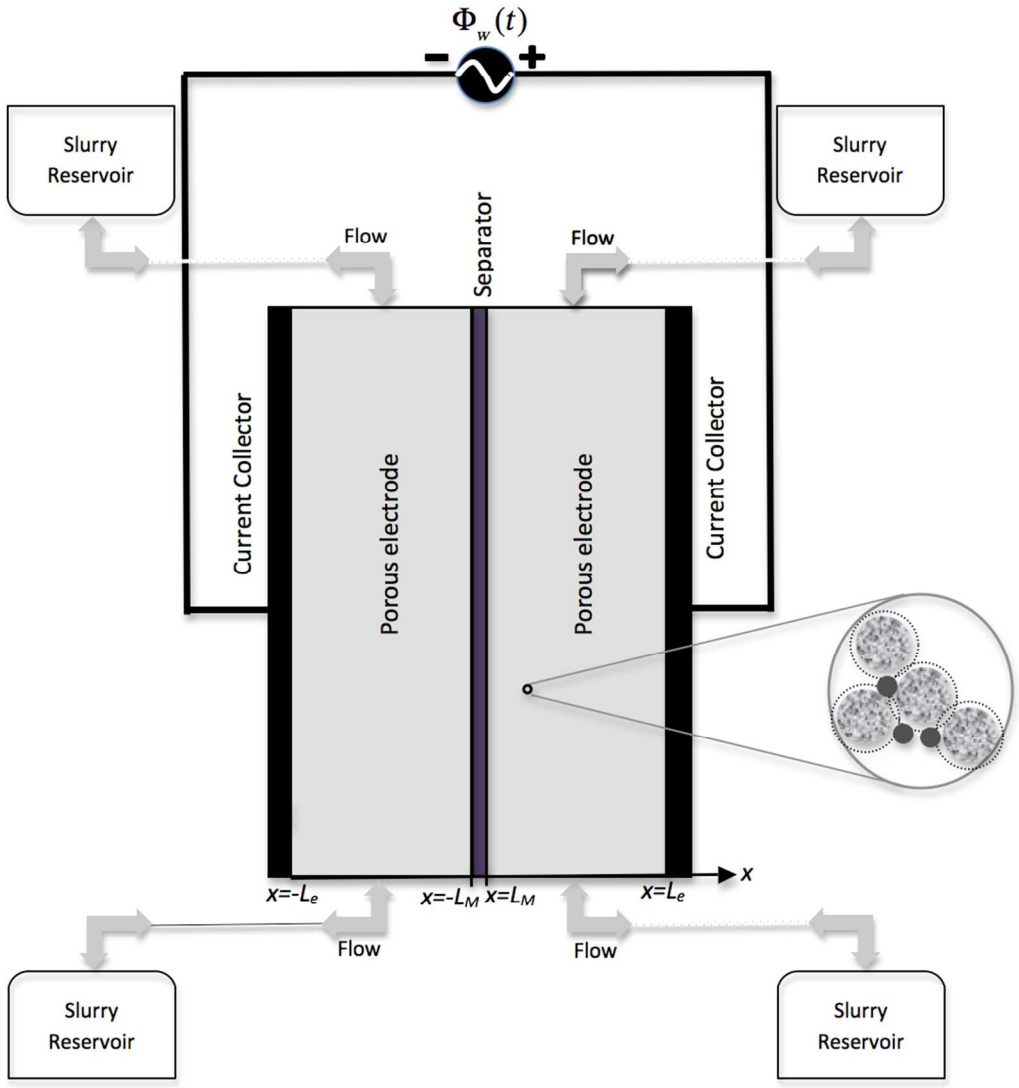

Figure 1: A schematic of the electrochemical flow capacitor / desalinator (EFC) system [13]. To store energy, the slurries are charged in the flow cell and then stored in separate reservoirs. To recover the stored energy, the charged slurries are pumped back into the liquid cell and discharged. The left and right current collectors are subject, respectively, to applied potentials $-\Phi_w/2$ and $\Phi_w/2$.

desorption step, in which the porous electrodes are regenerated. In contrast to CDIs, EFCs facilitate continuous operation without a need to interrupt the process for regeneration, and the particles with the immobilized salt ions can be either discharged to waste or regenerated remotely [24, 25, 31, 33, 34].

The EFCs can operate either in a continuous mode or in a "stop-and-go" mode. In the continuous mode, the particle slurry flows continuously through the system while

charging/discharging. While in the "stop-and-go" mode, the system is filled with a fresh load of particles, time is allowed for particle aggregation and charge transfer, and then the charged/discharged slurry is replaced. This operation is similar to that of conventional ECs with the added benefit of decoupling of power capacity and energy storage. For the present study, we will focus our attention on the "stop-and-go" mode where there is no flow of the porous electrodes.

In this paper, we use volume averaging to model the porous electrode. The volume-averaging (homogenization) theory of ion transport in porous electrodes was first developed by Newman and co-workers [18, 20, 26, 27]. Biesheuvel and Bazant [17] applied this theory to study the dynamics of capacitive charging and desalination of a half cell, consisting of a highly (infinitely) conductive, single porous electrode in contact with a stagnant electrolyte. Biesheuvel et al. [28] extended this work to account for Faradaic reactions at the electrodes' surfaces and overlapping electric double layers in nanoscale pores. Mirzadeh et al. [32] explored effects of surface conduction in accelerating the charging dynamics of porous electrodes. Zhao et al [29] studied experimentally and theoretically selective absorption of bivalent ions over monovalent ions during capacitive charging, and Rica et al [30] modeled capacitive extraction of energy from two streams with different salinities. All the studies to date focused on the limiting case of porous matrices with infinite electric conductivities. This is appropriate for monolithic electrodes. But, when the solid matrix is formed by particle aggregation, like in the EFC, contact resistance among the particles renders the electric conductivity finite. For example, the solid matrix conductivity in the semi-solid lithium rechargeable flow battery is as low as $\sim 0.001\ \mathrm{Sm}^{-1}$ [11]. Although with an appropriate design higher conductivities of the solid matrix are feasible, the above example demonstrates the need to study the dynamics of systems with finite solid matrix conductivities.

Here, we consider the charging dynamics of the EFC cell depicted in Fig. 1. The porous electrodes are inert and ideally polarizable. The electric double layers next to the pore surfaces are thin compared to the typical pore dimensions. We focus on a dilute, binary electrolyte and use the Gouy-Chapman-Stern model of the double layer. We first outline the mathematical model based on the volume averaging (homogenization) theory for porous electrodes and then explore the charging dynamics of the EFC when subjected to a step change in the collecting plates' potentials. In this model, we neglected the effect of surface conduction since it is not significant for

electrodes derived from activated carbon whose surface morphologies have breaks in the charge direction, as observed in [32]. We examine solid matrices with both infinite and finite electric conductivities and account for transport in the separator. The mathematical models are, respectively, solved analytically and numerically when the applied potentials are small and finite. The analysis of the infinitely-conductive matrix extends the work of Biesheuvel and Bazant [17] and provides a limiting case to verify the results of the finite-conductivity case. The analysis of the finite-conductivity matrix is entirely new and reveals the existence of an optimal value for the matrix conductivity.

2. Mathematical Model

Consider a granular medium saturated with an electrolyte solution and confined between two long, parallel, current-collecting plates spaced a distance $2L_e$ apart (Fig. 1). The granular medium is separated into two sections with an ion-permeable, electrically insulating, $2L_M$-thick spacer. The particles are porous (typically, amorphous carbon) and assemble by aggregation. The resulting solid porous matrix has an electrical conductivity of σ_m. The Debye screening length (λ_D) is small compared to the characteristic size of the pores (h_p). We model the aggregates as two porous electrodes.

To alleviate the need to model the complex geometry of the aggregate, we use volume-averaging (homogenization) [18]. Briefly, the field equations are averaged over a representative volume that is large compared to the characteristic pore size (h_p), but small compared to the size of the device (L_e), to yield conservation equations for the mean-field variables. In other words, we disregard the details of the geometry and endow the medium with "macroscopic," apparent properties such as porosity φ. To the first order of approximation, we assume that the porosity is independent of time and uniform in space. The electrical potentials in the solid, porous matrix and in the electrolyte are denoted, respectively, $\Phi_m(\mathbf{X},\tau)$ and $\Phi_e(\mathbf{X},\tau)$, where $\mathbf{X}$ is the position vector and τ is time. We adapt the convention that **bold** fonts and regular fonts represent, respectively, vectors and scalars. The subscripts *m* and *e* denote, respectively, variables associated with the solid matrix and the electrolyte solution that saturates the porous electrodes. The two granular media are in electrical contact with the corresponding collecting plates. The interface between the

solid matrix and the electrolyte is perfectly polarizable (blocking), and no Faradaic reactions take place at any solid-liquid interfaces. All the interactions between the solid matrix and the electrolyte are capacitive.

We consider the binary electrolyte $M^{z1}A^{z2}$, where M and A represent, respectively, cations of valence z_1 and anions of valence z_2. For example, in their flow capacitor, Presser et al [13] used Na_2SO_4 as the solute. In our notation, M will stand for Na ($z_1 = 1$) and A for SO_4 ($z_2 = -2$). The concentrations (mol/m^3) of M^{z1} and A^{z2} are denoted, respectively, C_1 and C_2. The pore-averaged mass fluxes are:

$$\mathbf{N}_i = \mathbf{u}C_i - D_i^*\nabla C_i - \frac{D_i^* z_i F}{R_u T} C_i \nabla \Phi_e \,, \qquad (i = 1, 2)\,. \tag{1}$$

In the above, $\mathbf{u}$ is the velocity vector; D_i^* is the apparent diffusion coefficient that accounts for hindered diffusion in the pores; R_u is the universal gas constant; T is the absolute temperature; and F is the Faraday constant. The three terms on the right hand side of equation (1) represent, in order, fluxes due to advection, diffusion, and electro-migration.

Since supercapacitors typically operate with relatively high salt concentrations, the Debye screening length $\lambda_D = \sqrt{\varepsilon R_u T/(F^2 \sum_i C_i z_i^2)}$ is small. In the above, ε is the solvent permittivity. For example, in the case of the 1M Na_2SO_4 aqueous solution [13], λ_D~0.2 nm, while the characteristic pore size (h_p) within the porous particles is around 2 nm [24] and between the particles on the order of micrometers. Outside the thin electric double layers, electro-neutrality prevails.

$$z_1 C_1 + z_2 C_2 = 0 \ . \tag{2}$$

The volume-averaged equation for the conservation of species is [20]:

$$\frac{\partial C_i}{\partial \tau} = -\nabla \cdot \mathbf{N}_i - a_s \dot{S}_i \,, \quad (i = 1,2). \tag{3}$$

In the above, $\dot{S}_i(\mathbf{X}, \tau)$ is the average rate of absorption of ion i by the EDL per unit interfacial area and a_s is the interfacial area per unit volume. Consistent with volume averaging, $a_s \dot{S}_i$ appears as a sink term in the mass conservation equation (3).

For brevity, we consider the special case when the cations and the anions have similar diffusivities. $D_1^* = D_2^* = D$. Adding equation (3) for the cations and anions, and taking advantage of the electro neutrality (2), we have

$$\frac{\partial C}{\partial \tau} = -\mathbf{u}\cdot\nabla C + D\nabla^2 C - a_s \dot{W} \quad , \tag{4}$$

where $C = (C_1 + C_2)/2$ is the average ion concentration and $\dot{W} = dW/d\tau = \left(\dot{S}_1 + \dot{S}_2\right)/2$ is the rate of ion accumulation in the EDL. Next, multiplying equation (3) for the cations by z_1 and equation (3) for the anions by z_2, and adding the resulting equations, we obtain

$$\nabla\cdot(\sigma_e \nabla\Phi_e) - a_s\dot{Q} = 0, \tag{5}$$

where $\sigma_e = \frac{-2DF^2 z_1 z_2}{R_u T} C$ is the effective conductivity of the electrolyte and $\dot{Q} = dQ/d\tau = F\left(z_1\dot{S}_1 + z_2\dot{S}_2\right)$ is the rate of charge accumulation in the EDL.

In the solid porous matrix, the volume-averaged Ohm's law is:

$$\nabla\cdot(\sigma_m \nabla\Phi_m) + a_s\dot{Q} = 0, \tag{6}$$

where σ_m is the electric conductivity of the solid matrix. Witness that the rate of charge accumulations in the solid and in the EDL are equal in magnitude and opposite in sign.

We neglect steric-hindrance and assume that the EDL is at quasi-equilibrium, i.e., the ion concentrations in the EDL is given by the Gouy-Chapman-Stern (GCS) theory [15, 16]. The local potential difference between the matrix and the electrolyte is the sum of the potential drops across the Stern layer and the diffuse layer.

$$\Phi_m - \Phi_e = \Delta\Phi_s + \Delta\Phi_D \ . \tag{7}$$

For conciseness, we focus on a symmetric electrolyte ($z_1 = -z_2 = z$).

$$Q = -\sqrt{8\varepsilon R_u T C}\,\sinh\left(\frac{Fz\Delta\Phi_D}{2R_u T}\right). \tag{8}$$

In the Stern layer, $\Delta\Phi_S = -C_S Q$, where $C_s = \varepsilon/\lambda_s$ is the Stern layer capacitance and λ_s is the Stern layer's thickness. Similarly, the ion accumulation in the EDL

$$W = \frac{\sqrt{8\varepsilon R_u T C}}{Fz}\,\sinh^2\left(\frac{Fz\Delta\Phi_D}{4R_u T}\right). \tag{9}$$

The separation spacer is insulating. To the first order of approximation, we neglect any ion absorption in the spacer's pores. Therefore, the equations for the ion concentration and the potential of the electrolyte residing in the spacer are similar to equations (4) and (5) without any source terms and with an apparent diffusion coefficient D_M appropriate for the spacer pores, which may differ from the diffusion coefficients of the ions in the electrolyte.

At the collecting plates, the ionic fluxes $\hat{\mathbf{n}} \cdot \mathbf{N}_i = 0$, where $\hat{\mathbf{n}}$ is an outer unit vector normal to the solid surface. The collecting plates' potentials are externally controlled. At the insulating spacer surface, $\hat{\mathbf{n}} \cdot \nabla \Phi_m = 0$.

Here, we focus on a quiescent slurry $\boldsymbol{u} = 0$. In the context of an energy storage device, we envision that the space between the two collecting plates is filled with the slurry when the electrodes are disconnected from a power source / load. The solid particles aggregate to form interconnected networks, facilitating electron transport among the particles. At time $t = 0$ (once the particles have aggregated), the collecting plates are connected to an external power source / load. Under the afore-described circumstances, the problem is modeled as one-dimensional in the spatial coordinate (X). A similar problem was considered by Biesheuvel and Bazant [17] for the limiting case of a solid matrix with infinite conductivity in the absence of a separator. When the solid matrix forms by aggregation, like in our case, finite matrix conductivity must be considered.

Next, we recast the equations in a dimensionless form. We adopt the convention that lower case letters are the dimensionless equivalent of the dimensional quantities denoted with capital letters. L_e is the length scale; $\delta_p L_e^2/D$ is the time scale; the initial concentration C_0 is the concentration scale; the thermal potential $R_u T/zF$ is the potential scale; $2DFzC_0/L_e$ is the current scale; $2DF^2z^2C_0/R_uT$ is the conductivity scale; $\delta_p = a_s\lambda_D = \varphi\lambda_D/h_p$ is the volume fraction occupied by the EDL; φ is the average porosity; $h_p = \varphi/a_s$ is the average pore size; $\lambda_D = \sqrt{\varepsilon R_u T/(2F^2z^2C_0)}$ is the Debye screening length; and $\delta_M = L_M/L_e$ is the relative thickness of the separator.

Neglecting the Stern layer ($\lambda_s \sim 0$) and substituting (9) and (8) into (4) and (5), we have

$$\frac{\partial c}{\partial t} = \delta_p M_\alpha \frac{\partial^2 c}{\partial x^2} - M_s \delta_p \frac{\partial}{\partial t}\left[4\sqrt{c}\,\sinh^2\left(\frac{\phi_m - \phi_e}{4}\right)\right] \tag{10}$$

and

$$M_\alpha \frac{\partial}{\partial x}\left(c\frac{\partial \phi_e}{\partial x}\right) + M_s \frac{\partial}{\partial t}\left[2\sqrt{c}\,\sinh\left(\frac{\phi_m - \phi_e}{2}\right)\right] = 0\,, \tag{11}$$

where $M_s = M_\alpha = 1$ in the electrolyte ($\delta_M \le |x| \le 1$) and $M_s = 0$ and $M_\alpha = \alpha = D_M/D$ in the spacer region ($|x| < \delta_M$). Similarly, equation (6) assumes the form

$$\frac{\partial}{\partial x}\left(\sigma\frac{\partial \phi_m}{\partial x}\right) - \frac{\partial}{\partial t}\left[2\sqrt{c}\,\sinh\left(\frac{\phi_m - \phi_e}{2}\right)\right] = 0 \tag{12}$$

in the electrolyte ($\delta_M \le |x| \le 1$). In (12), $\sigma = \sigma_m R_u T/(2DF^2 z^2 C_0)$ is the dimensionless conductivity of the solid matrix.

As for the boundary conditions, the current collecting plates ($x = \pm 1$) are impermeable and blocking:

$$\frac{\partial c}{\partial x} = \frac{\partial \phi_e}{\partial x} = 0\,. \tag{13}$$

We neglect contact resistance between the matrix and the collecting plates. Thus, the solid matrix next to the plates has the same potential as the adjacent collecting plate.

$$\phi_m(\pm 1, t) = \pm\frac{\phi_w(t)}{2}\,. \tag{14}$$

Since the separator is electrically insulating,

$$\frac{\partial \phi_m(\pm\delta_M, t)}{\partial x} = 0\,. \tag{15}$$

The initial conditions are:

$$c(x,0) - 1 = \phi_e(x,0) = \phi_m(x,0) = 0\,. \tag{16}$$

The equations and boundary conditions suggest that the instantaneous concentration field is symmetric and that the potential fields must be anti-symmetric with respect to $x = 0$.

$$c(-x,t) = c(x,t),\ \phi_e(-x,t) = -\phi_e(x,t), \text{ and } \phi_m(-x,t) = -\phi_m(x,t).$$

Thus,

$$\frac{\partial c(0,t)}{\partial x} = \phi_e(0,t) = 0\,. \tag{17}$$

Therefore, it is sufficient to consider only one half of the domain, i.e., $0 \le x \le 1$.

The external current supplied per unit area of the current collectors,

$$i_c = -\left(\sigma \frac{\partial \phi_m}{\partial x}\right)_{x=1} = -\frac{\partial}{\partial t} \int_{\delta_M}^{1} 2\sqrt{c} \sinh\left(\frac{\phi_m - \phi_e}{2}\right) dx, \tag{18}$$

is obtained by integrating equation (12) across the domain occupied by the electrolyte ($\delta_M \le x \le 1$). The total charge accumulated in one half of the electrochemical reactor over the time interval $[0, t]$,

$$q(t) = -\int_0^t i_c dt = \int_{\delta_M}^{1} 2\sqrt{c} \sinh\left(\frac{\phi_m - \phi_e}{2}\right) dx, \tag{19}$$

is equal to the total charge stored in the EDL as given by the expression (8). We use $2FzC_0\delta_p L_e$ as the charge scale. The charge stored in the other half of the reactor is of the same magnitude and opposite sign.

When we consider desalination, the average electrolyte salt concentration as a function of time is of interest. By integrating equation (10) over the half reactor $0 \le x \le 1$ and over the time interval $[0, t]$, we have

$$\bar{c}(t) = \int_0^1 c(x,t) dx = 1 - \delta_p \int_{\delta_M}^{1} 4\sqrt{c} \sinh^2\left(\frac{\phi_m - \phi_e}{4}\right) dx. \tag{20}$$

When the potential drop across the EDL is large ($\phi_m - \phi_e \gg 1$),

$$\sinh\frac{\phi_m - \phi_e}{2} \approx \frac{1}{2}\exp\left(\frac{\phi_m - \phi_e}{2}\right) \approx 2\left(\sinh\frac{\phi_m - \phi_e}{4}\right)^2,$$

$$\bar{c}(t) \approx 1 - \delta_p q(t), \tag{21}$$

and the average bulk solution concentration and charge accumulation behave similarly.

In the limiting case of a highly conductive solid matrix ($\sigma \to \infty$),

$$\phi_m(x,t) = \mathrm{sgn}(x)\, \phi_w(t)/2 \tag{22}$$

and the initial conditions for the potentials are

$$\phi_e(x,0) = \phi_m(x,0) = \mathrm{sgn}(x)\,\phi_w(0)/2. \tag{23}$$

3. Results and Discussion

We consider the case when the current collecting electrodes are subjected to the step change in potential

$$\phi_w(t) = \phi_p H(t), \tag{24}$$

where $H(t)$ is the Heaviside step function ($H(t) = 0$ when $t < 0$ and $H(t) = 1$ when $t \geq 0$) and ϕ_p is the magnitude of the potential-step. We will examine a solid matrix with an infinite and a finite electric conductivity. The case with infinite matrix conductivity was considered previously in [17], albeit in the absence of the separation. The results presented here are applicable to both energy storage devices (supercapacitors) and desalinators.

3.1 Steady-State

We first examine the longtime, steady-state solution. After sufficient time, the solid matrix will assume the potential of the collecting plate with which it is in contact. Once the EDL forms, it will screen the bulk of the electrolyte from the solid matrix. Equations (10-12) admit the steady state solution:

$$\phi_e(x,\infty) = 0,\ \phi_m(x,\infty) = \mathrm{sgn}(x)\,\phi_p/2\ \text{, and } c(x,\infty) = c_\infty. \tag{25}$$

The equilibrium electrolyte concentration,

$$\sqrt{c_\infty} = -2\delta_p(1-\delta_M)\sinh^2\left(\frac{\phi_p}{8}\right) + \sqrt{4\delta_p^2(1-\delta_M)^2\sinh^4\left(\frac{\phi_p}{8}\right)+1}, \tag{26}$$

is obtained by evaluating the integral in (20) with the steady state potentials given in (25). When $\phi_p \ll 1$,

$$c_\infty \approx 1 - \frac{1}{16}\delta_p(1-\delta_M)\phi_p^2 + O\left(\phi_p^4\right)\ .$$

When ϕ_p>>1,

$$c_\infty \approx \frac{e^{-\phi_p/2}}{\delta_p^2(1-\delta_M)^2}\ .$$

As ϕ_p increases, c_∞ decreases exponentially. Eventually, for a sufficiently large ϕ_p, the ions will be completely depleted from the electrolyte solution. When the electrochemical cell operates as a desalinator, c_∞ is the salt concentration remaining in the solvent after a long time.

The maximum charge storage capacity (19) per unit area of the current-collecting electrode is attained when the system reaches a steady state.

$$q_\infty = q(\infty) = 2\sqrt{c_\infty}(1-\delta_M)\sinh\left(\frac{\phi_p}{4}\right). \tag{27}$$

When ϕ_p is small,

$$q_\infty \approx 2(1-\delta_M)\sinh\left(\frac{\phi_p}{4}\right). \tag{28}$$

When $\phi_p \gg 1$,

$$q_\infty \approx \frac{1}{\delta_p}. \tag{29}$$

The large ϕ_p limit corresponds to

$$Q_\infty = 2FzC_0\delta_p L_e q_\infty = 2FzC_0 L_e, \tag{30}$$

indicating that all the ions have been packed into the EDL. This is, of course, a theoretical result as it ignores steric hindrance.

Fig. 2 depicts the steady state concentration c_∞ (a) and the charge storage density q_∞ (b) as functions of ϕ_p when δ_p =0.001, 0.01, and 0.1. The plateaus in (b) indicate that once a certain value of $\phi_{p,c}$ is exceeded, most of the available charge has accumulated in the EDL and any further increase in ϕ_p results in diminishing returns. The predictions for large ϕ_p may be of only theoretical value as overcrowding in the EDL may render the Gouy-Chapman theory invalid and one may need to account for steric effects [21, 22].

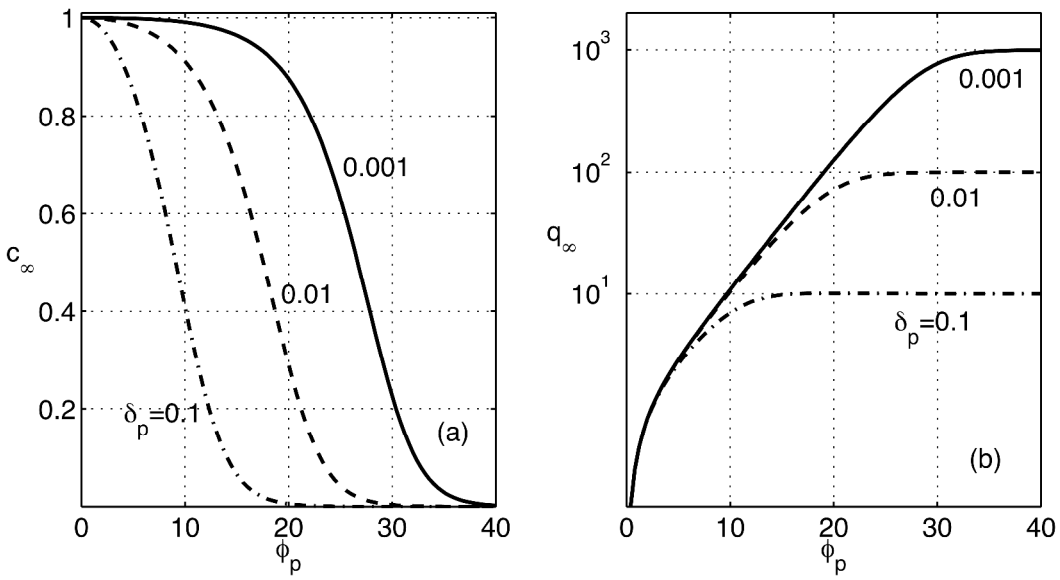

Figure 2: The equilibrium concentration c_∞ (a) and the stored charge q_∞ (b) as functions of the applied potential ϕ_p. $\delta_p = 0.001, 0.01$, and 0.1. $\delta_M = 0.1$.

3.2 Solid Matrix with Infinite Electric Conductivity

When the electric conductivity of the solid matrices is large ($\sigma \to \infty$), the potential of each solid matrix is uniform and equals the potential applied to the corresponding, collecting-plate (eq. 22). When $t = 0$, the electrolyte confined in each porous electrode has the same potential as the adjacent solid matrix and the potential of the electrolyte in the separator varies linearly with *x*.

We first consider the case $\phi_p \ll 1$, linearize the equations, and obtain analytical solutions to gain insights into the process and obtain expressions that we can later use to verify our numerical solutions. When $\phi_p \ll 1$, the concentration $c(x,t) \sim 1$. The linear version of equation (11) is:

$$\frac{\partial^2 \phi_e}{\partial x^2} - M_s \frac{\partial \phi_e}{\partial t} = 0 \tag{31}$$

with the boundary conditions

$$\frac{\partial \phi_e}{\partial x}(1,t) = \phi_e(0,t) = 0 \tag{32}$$

and the initial conditions $\phi_e(x,0) = \phi_p x/2\delta_M$ when $0 \le x \le \delta_M$ and $\phi_e(x,0) = \phi_p/2$ when $\delta_M \le x \le 1$. Since within the separator region ($0 \le x \le \delta_M$) equation (11) reduces to $\partial^2\phi_e/\partial x^2 = 0$, we have

$$\phi_e(x,t) = \phi_e(\delta_M,t)\frac{x}{\delta_M} \quad \text{when } 0 \le x \le \delta_M. \tag{33}$$

At the interface between the porous electrode and the separator,

$$[\phi_e]_{x=\delta_M^+} - [\phi_e]_{x=\delta_M^-} = \left[\frac{\partial\phi_e}{\partial x}\right]_{x=\delta_M^+} - \alpha\left[\frac{\partial\phi_e}{\partial x}\right]_{x=\delta_M^-} = 0, \tag{34}$$

where δ_M^+ and δ_M^- denote, respectively, the porous electrode side and the separator side of the interface. Accordingly, the potential ϕ_e right outside the interface satisfies the Robins boundary condition

$$\frac{\partial\phi_e(\delta_M^+,t)}{\partial x} = \alpha\frac{\phi_e(\delta_M^+,t)}{\delta_M}. \tag{35}$$

Within $\delta_M \le x \le 1$, the solution to (31) is

$$\frac{\phi_e(x,t)}{\phi_p/2} = \sum_{n=1}^{\infty}\frac{4\sin\lambda_n}{\sin(2\lambda_n)+2\lambda_n}e^{-\left(\frac{\lambda_n}{1-\delta_M}\right)^2 t}\cos\left(\lambda_n\frac{1-x}{1-\delta_M}\right), \tag{36}$$

where the eigenvalues λ_n are the roots of the equation

$$\lambda_n\tan(\lambda_n) = \alpha\frac{1-\delta_M}{\delta_M} = \beta. \tag{37}$$

As $n \to \infty$, $\lambda_n \to n\pi$ and the series (36) converges rapidly. The parameter β can be interpreted as the ratio of the resistance to mass flow through the cell, $\sim(1-\delta_M)$, and through the separator, $\sim\delta_M/\alpha$.

For later use, we express explicitly the leading eigenvalue λ_1 in terms of β in a form appropriate for large β,

$$\lambda_1 \sim \frac{\pi}{2}\left(1 - \frac{1}{\beta} + \frac{1}{\beta^2} - \frac{12-\pi^2}{12\beta^3} - \frac{\pi^2-3}{3\beta^4}\right) + O(\beta^{-5}), \tag{38}$$

and for small β,

$$\lambda_1 \sim \sqrt{\beta}\left(1 - \frac{1}{6}\beta + \frac{11}{360}\beta^2 - \frac{17}{5040}\beta^3\right) + O(\beta^{9/2}). \tag{39}$$

We provide a similar expansion in terms of δ_M,

$$\lambda_1 \sim \frac{\pi}{2}\left(1 - \frac{1}{\alpha}\delta_M + \frac{(1-\alpha)}{\alpha^2}\delta_M^2 - \frac{\pi^2 - 12(1-\alpha)^2}{12\alpha^2}\delta_M^3\right) + O(\delta_M^4)\,.$$

Substituting (36) into the linearized version of (19), we find the charge accumulation over half of the cell,

$$q(t) \approx \int_{\delta_M}^{1} (\phi_m - \phi_e)dx = q_\infty - \phi_p \sum_{n=1}^{\infty} \frac{2\sin^2\lambda_n}{\sin(2\lambda_n) + 2\lambda_n} \frac{1-\delta_M}{\lambda_n} e^{-\left(\frac{\lambda_n}{1-\delta_M}\right)^2 t}, \qquad (40)$$

as a function of time.

Next, we solve the nonlinear equations (10-12) with the weak form PDE model of the multiphysics, finite element program COMSOL™. Various mesh sizes and time-steps are tested and grid-size independence is verified. Fig. 3 compares the computed potential $\phi_e(x,t)$ distribution and accumulated charge $q(t)$ with the analytical expressions when $\phi_p = 0.4$, $\alpha = 0.5$, and $\delta_M = 0.1$. Since the series (36) converges rapidly, only 15 terms are needed to achieve sufficient precision. The finite element solution is in excellent agreement with the analytical

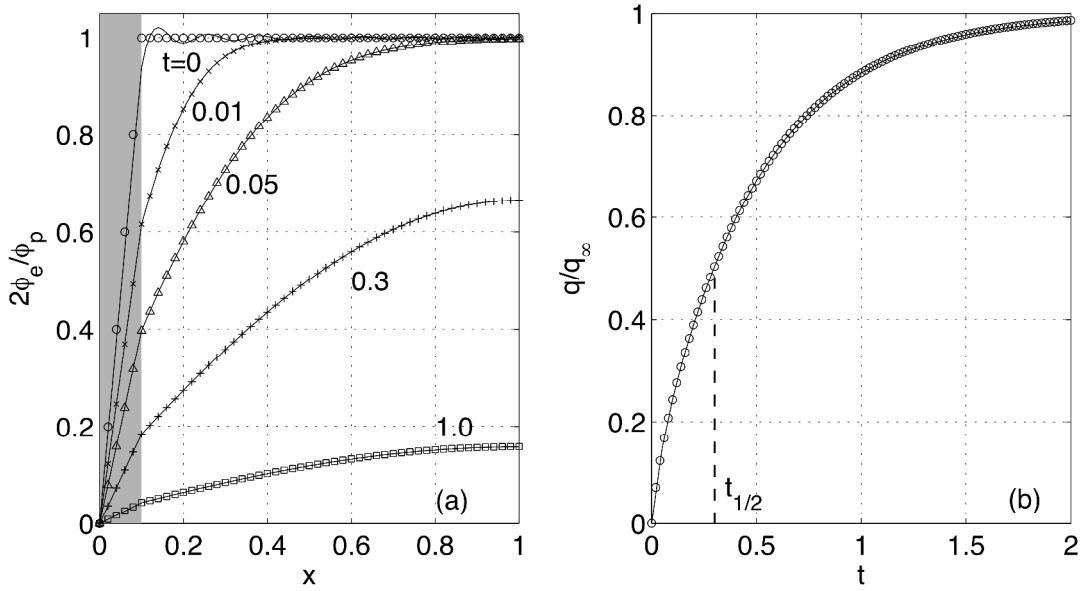

Figure 3: (a) The normalized electrolyte potential $2\phi_e/\phi_p$ as a function of position at various times $t = 0(\odot)$, $0.01(\times)$, $0.05(\triangle)$, $0.3(+)$, and $1(\square)$ and (b) the accumulated charge q/q_∞ as a function of time. Solid lines and symbols correspond, respectively, to the (15 term) analytical and finite element solutions. $\phi_p = 0.4$, $\delta_p = 0.005$, $\delta_M = 0.1$, and $\alpha = 0.5$. The gray slab indicates the region occupied by the separator.

solution with the exception of short times when the analytical solution exhibits the Gibbs phenomenon due to the discontinuity in the potential's gradient next to the separator's surface ($x = \delta_M$). The analytical solution (36) provides reasonable results as long as $\phi_p < 5$.

Figs. 4a and 4b depict, respectively, the computed potential and concentration distributions of the electrolyte as functions of position at various times. $\phi_p = 40$, $\delta_M = 0.05$, and $\alpha = 0.5$. When the potential difference was first applied to the current collecting plates ($t = 0$), both the solid matrix and the electrolyte solution in the pores ($\delta_M < x < 1$) assumed uniform potentials equal to the collecting plate's potential $\phi_p/2$. In the insulating spacer ($\lfloor x \rfloor < \delta_M$), the electrolyte potential varied linearly. At very early times, the electric field was present only in the separator's vicinity, causing nearby anions to migrate through the separator in the positive *x*-direction and cations in the opposite direction. In the right half cell, the translocated anions, as well as anions from the pore electrolyte, accumulated in the EDLs and screened the surfaces of the pores, enabling the electric field to further diffuse into the half cell (Fig. 4a). Fig. 4b depicts the accompanying depletion in the solute concentration. Eventually, a steady state was established. At steady state, both the electrolyte potential and the solute concentration attain the uniform values $\phi_e = 0$ and $c_\infty = 9 \times 10^{-5}$. Half of the total anions stored in the EDL of the right half cell came

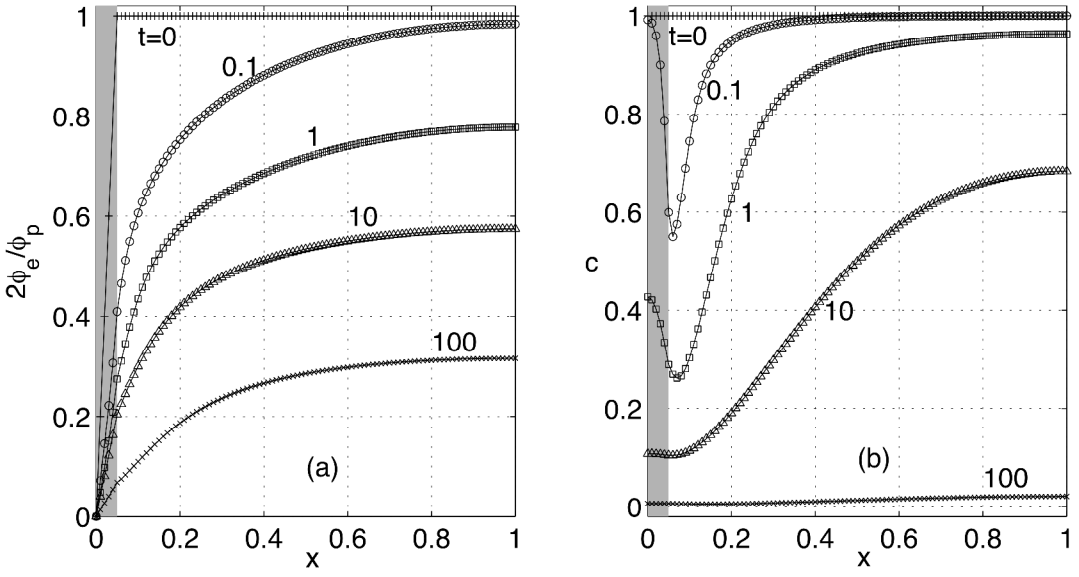

Figure 4: The normalized electrolyte potential $2\phi_e/\phi_p$ (a) and the solute concentration (b) as functions of position *x* at times $t = 0$(+), 0.1(⊙), 1(□), 10(△), and 100(×). $\phi_p = 40, \delta_p = 0.005$, $\delta_M = 0.05$, and $\alpha = 0.5$. The gray slab represents the separator.

from the left half cell and migrated through the insulating spacer. At the relatively high potential of Fig. 4, the solvent is nearly completely depleted of the solute. If such an electrochemical reactor were used as a desalinator, over 99.99% of the salt content would have been removed from the brine.

Fig. 5 depicts the accumulated charge $q(t)$, the average solute concentration $\bar{c}(t)$, and the solute concentration next to the separator's surface $c(\delta_M, t)$ as functions of time for various

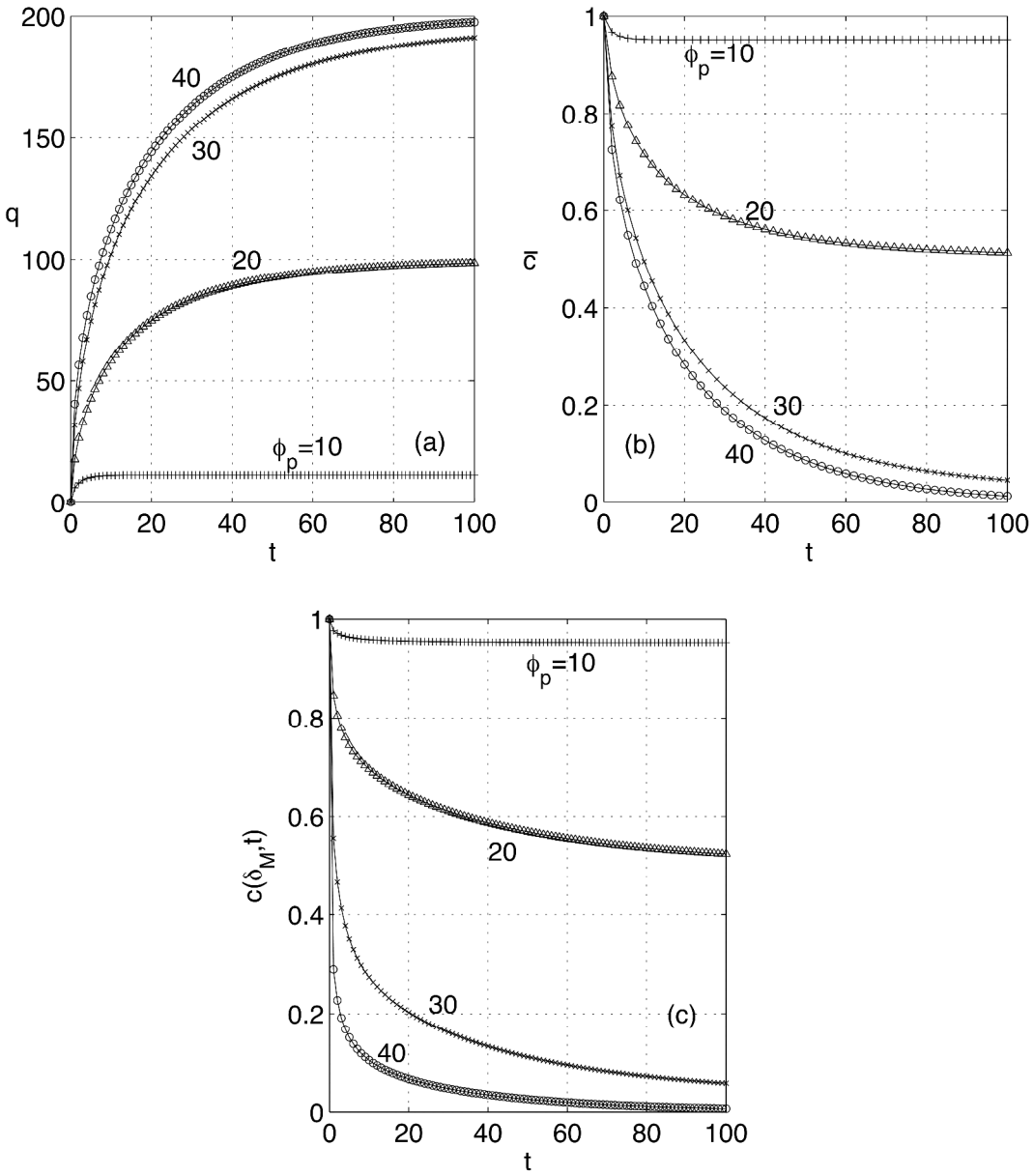

Figure 5: The accumulated charge $q(t)$ (a), the average solute concentration $\bar{c}(t)$ (b), and the solute concentration (δ_M,t) next to the separator's surface (c) as functions of time. ϕ_p =10(+), 20(△), 30(×), and 40(⊙). $\delta_p = 0.005$, $\delta_M = 0.05$, and α =0.5.

applied potentials. As time increases, both the accumulated charge and the solute concentrations approach monotonically their equilibrium values. Due to the ion depletion next to the separator at high potentials, the solute concentration at the separator reduces at a faster rate than the average concentration. When $\phi_p = 10$, 20, 30, and 40; the corresponding accumulated charges are $q_\infty = 11.22$, 100.24, 197.57, and 200.00; and the respective steady state concentrations are $c_\infty = 0.95$, 0.51, 0.01, and 9×10^{-5}. The data in Fig. 5 satisfies the relationship $q(t)/q_\infty \approx \big(1-\bar{c}(t)\big)/(1-c_\infty)$, consistent with equation (21), as demonstrated in Fig. 6.

As a figure of merit to evaluate the charging process, we use the time $t_{1/2}$ needed for the accumulated charge $q(t)$ to reach half of its equilibrium value. $q\big(t_{1/2}\big) = 0.5q_\infty$. When ϕ_p is small, we obtain (with equations 40, 28, and expansions 38 and 39):

$$t_{1/2} = \left(\frac{1-\delta_M}{\pi}\right)^2 \left(8ln\left(\frac{4}{\pi}\right)\left(\frac{\beta+1}{\beta}\right)^2 + \frac{4}{\beta} + \frac{6-\pi^2}{\beta^2}\right) + O(\beta^{-3}) \qquad (41)$$

for large β , and

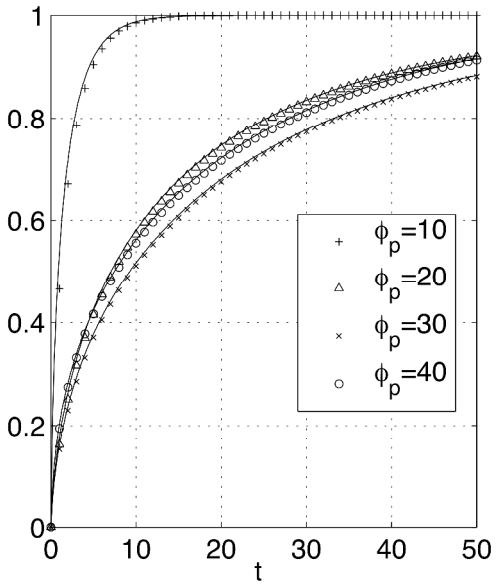

Figure 6: Comparison of the normalized charge accumulation $q(t)/q_\infty$ (solid line) with $\big(1-\bar{c}(t)\big)/(1-c_\infty)$ (symbols) when ϕ_p =10(+), 20(△), 30(×), 40(⊙). $\delta_p = 0.005$, $\delta_M = 0.05$ and α =0.5.

$$t_{1/2} = (1-\delta_M)^2\left(\frac{ln(2)}{\beta}+\frac{ln(2)}{3}-\frac{1-ln(2)}{45}\beta\right)+O(\beta^2) \quad (42)$$

for small β. When $\beta \gg 1$, the ions' electro-migration across the separator is very efficient and the charging process is limited by the ions' mass transfer in the pore electrolyte. Since $q_\infty \sim (1-\delta_M)\phi_p$ (equation 28) and the rate of mass transport in the half cell is proportional to $\bar{c}\phi_p/(1-\delta_M)$, we expect the characteristic charging time to scale like $q_\infty/\left(\bar{c}\phi_p/(1-\delta_M)\right) \sim (1-\delta_M)^2$, which is consistent with the leading term in (41). When $\beta \ll 1$, the rate of the ions' electro-migration across the separator, $\alpha\bar{c}\,\phi_p/\delta_M$, is the controlling factor and the charging time is expected to scale like $q_\infty/\left(\alpha\bar{c}\,\phi_p/\delta_M\right) \sim \delta_M(1-\delta_M)/\alpha$, which is consistent with the leading term of (42). As α decreases, β decreases, and the separator's resistance to mass transfer and the charging time $t_{1/2}$ increase.

Fig. 7 depicts the characteristic charging time $t_{1/2}$ as a function of δ_M (a), α (b), and ϕ_p (c). The symbols, dash, and dash-dot lines correspond to finite element calculations, large β predictions (41), and small β predictions (42). Fig. 7a depicts $t_{1/2}$ as a function of the separator thickness when the applied potential is small ($\phi_p = 0.4$). Witness the excellent agreement between the prediction (41) and the finite element calculations. In the limit of small separator thickness $\delta_M \ll 1$, equation (41) reduces to $t_{1/2} \sim 0.196\left[1+\left(\frac{4.07}{\alpha}-2\right)\delta_M + O(\delta_M^2)\right]$. As δ_M increases, the separator resistance to mass transfer increases while the half cell resistance decreases. When $\alpha \leq 2.03$, the characteristic time $t_{1/2}$ increases as δ_M increases, as depicted in Fig. 7a for the case of $\alpha = 1$. This increase is brought about because for small α, the separator resistance increases faster than the half cell resistance decreases as δ_M increases. The opposite is true when $\alpha > 2.03$. Fig. 7b depicts $t_{1/2}$ as a function of the relative separator diffusion coefficient α. Not surprisingly, as α increases, the separator resistance to ion transport decreases and the characteristic charging time decreases as well. Here again, the asymptotic predictions of (41) and (42) agree well with the numerical results.

Fig. 7c depicts $t_{1/2}$ as a function of the applied potential difference ϕ_p for three different cases. We first discuss case A when $\delta_p = 0.005$, $\delta_M = 0.05$ and $\alpha = 0.5$ (circles). When $\phi_p \ll 1$, the numerical solution reproduces the predicted plateau of $t_{1/2} \approx 0.25$ (equation 41). As ϕ_p

increases $(4 \leq \phi_p \leq 25)$, $t_{1/2}$ increases exponentially due to the system's nonlinear, ϕ_p-dependent capacitance $\frac{q_\infty}{\phi_p} \sim \frac{2(1-\delta_M)}{\phi_p}\sqrt{c_\infty}\sinh\left(\frac{\phi_p}{4}\right)$, where c_∞ is given in equation (26). Based on our scaling arguments, we anticipate $t_{1/2} \sim \frac{2q_\infty(1-\delta_M)}{\phi_p}$, where we approximated $c_\infty \sim 1$. When ϕ_p increases beyond 25, $t_{1/2}$ peaks and then decreases slightly. The peak in $t_{1/2}$ occurs because the stored charge saturates at a sufficiently large ϕ_p, $q_\infty \approx 1/\delta_p$ (equation 29). Above this saturation potential, $t_{1/2} \sim \frac{2(1-\delta_M)}{\delta_p \phi_p}$. Based on equation (26), we estimate that $t_{1/2}$ peaks when $\sinh\left(\frac{\phi_p}{8}\right) \sim 1/\sqrt{2\delta_p(1-\delta_M)}$ or $\phi_p \approx 24.2$. At potentials above the peak potential, the decline in $t_{1/2}$ is because the rate of ion transfer increases as the applied potential increases. This decline is, however, slower than the estimated rate $\sim\phi_p^{-1}$ due to the severe ion depletion and ion transport blockage next to the insulating separator at large applied potential (i.e. $\phi_p = 40$, Fig. 4b). Cases B ($\delta_p = 0.005$, $\delta_M = 0.05$, and $\alpha = 1$; plus symbols) and C ($\delta_p = 0.001$, $\delta_M = 0.1$ and $\alpha = 1$; triangles) exhibit similar qualitative behaviour to case A (Fig. 7c). The charging times at low applied potentials are potential-independent, with $t_{1/2} \sim 0.21$ for case B and $t_{1/2} \sim 0.23$ for case C, consistent with the predictions of (41). In case B, the behaviour of $t_{1/2}$ follows closely that of case A, indicating that the doubling of the separator's diffusion coefficient has only a small effect on the charging time. In case C, the dependence of the charging time on the applied potential is qualitatively similar to cases A and B. The charging time peaks, however, at a larger potential and the peak is about five fold greater than in the previous two cases. This is a result of δ_p being five fold smaller in case C than in A and B, and is consistent with our scaling argument that $t_{1/2}$ is inversely proportional to δ_p. The computed potential at the peak $\phi_p \approx 31$ also agrees with the estimate of $\phi_p \approx 30.8$.

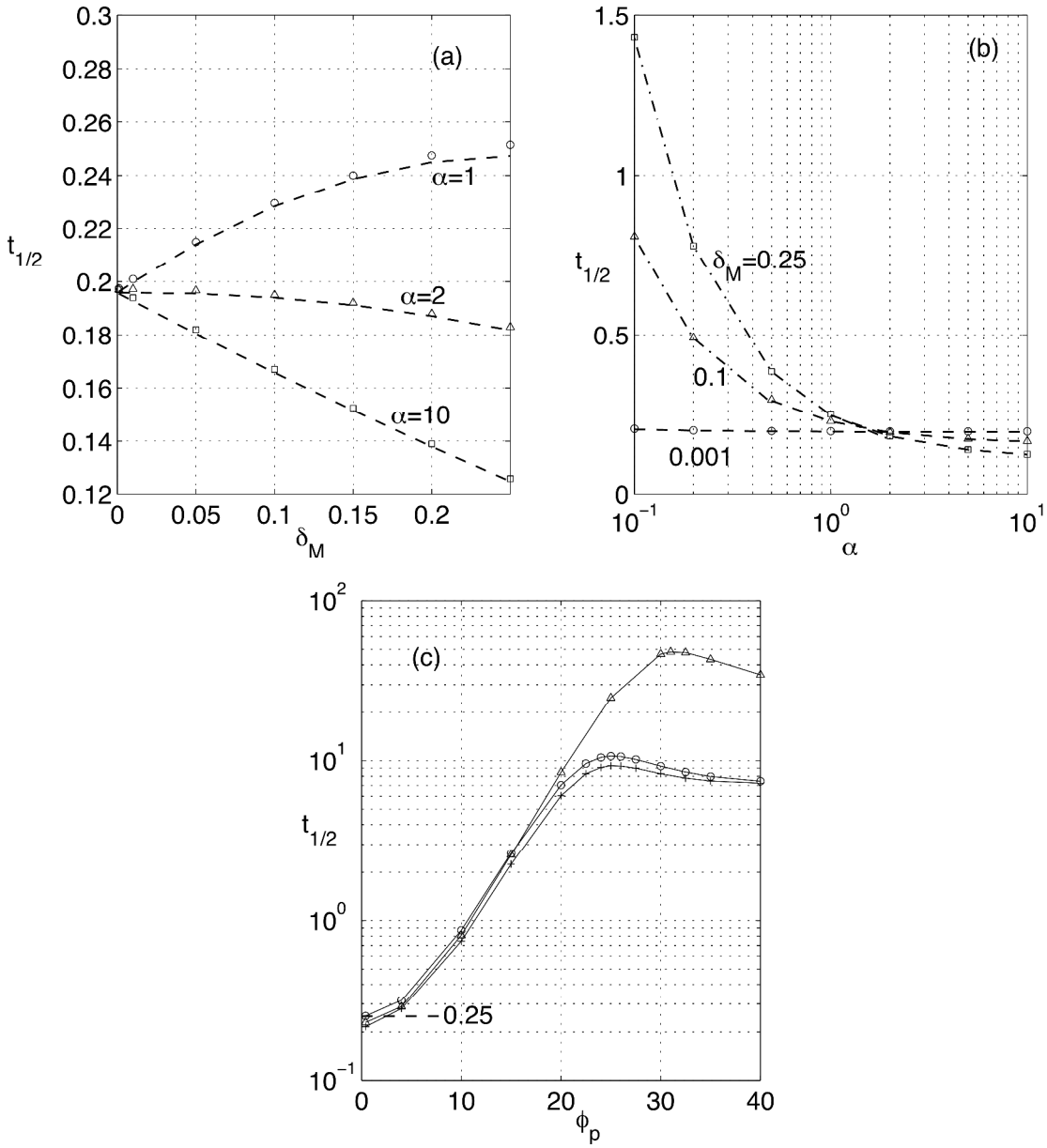

Figure 7: (a) The characteristic charging time $t_{1/2}$ as a function of δ_M. α =1(⊙), 2(△), and 10(□). ϕ_p =0.4 and δ_p =0.001. (b) $t_{1/2}$ as a function of α. δ_M =0.001(⊙), 0.1(△), and 0.25(□). ϕ_p =0.4 and δ_p =0.001. (c) $t_{1/2}$ as a function of ϕ_p. Case A: $\delta_p = 0.005$, $\delta_M = 0.05$, $\alpha = 0.5$ (⊙); case B: $\delta_p = 0.005$, $\delta_M = 0.05$, $\alpha = 1$ (+); and case C: $\delta_p = 0.001$, $\delta_M = 0.1$, $\alpha = 1$ (△). The symbols denote results of finite element calculations. The dash and dash-dot lines correspond, respectively, to the asymptotic predictions of (41) and (42). The solid lines in (c) were added to guide the eye.

3.3 Solid Matrix with Finite Electric Conductivity

When the solid matrix is formed by particle aggregation, the electric conductivity of the aggregate is likely to be finite and possibly lower than the electrolyte's conductivity. For example, in the semi-solid lithium rechargeable flow battery [11], the solid matrix conductivity ranged from 0.001 to $0.006\ \mathrm{Sm}^{-1}$ while the conductivity of the 1M Na_2SO_4 electrolyte was $\sim 4.0\ \mathrm{Sm}^{-1}$. Although with appropriate slurry design much greater solid matrix conductivities are anticipated, the above example demonstrates the need to examine the effects of solid matrix conductivity on a system's dynamics.

We first consider the case of a small potential $\phi_p \ll 1$, linearize the equations (10-12), and obtain analytical solutions. When $\phi_p \ll 1$, the concentration $c(x,t) \approx 1$. Equations (11) and (12) reduce, respectively, to

$$\frac{\partial^2 \phi_e}{\partial x^2} + \frac{\partial}{\partial t}(\phi_m - \phi_e) = 0\,, \tag{43}$$

and

$$\sigma \frac{\partial^2 \phi_m}{\partial x^2} - \frac{\partial}{\partial t}(\phi_m - \phi_e) = 0\,, \tag{44}$$

outside the separator region $\delta_M \le x \le 1$. The boundary conditions for ϕ_e are (13) and (35), and those for ϕ_m are (14) and (15). We combine equations (43) and (44) to form an equation for the zeta potential $\zeta = \phi_m - \phi_e$:

$$\frac{\partial \zeta}{\partial t} - \left(\frac{\sigma}{1+\sigma}\right)\frac{\partial^2 \zeta}{\partial x^2} = 0\,. \tag{45}$$

In the interest of space, we provide here solutions only for $\zeta(x,t)$. Note that the coefficient of the second term is comprised of the added resistivities of the electrolyte and solid matrix. The corresponding expressions for $\phi_m(x,t)$ and $\phi_e(x,t)$ can be similarly derived, but are not presented here.

We note that $\phi_e + \sigma\phi_m = A(t)x + B(t)$, which is useful for deriving the boundary conditions for ζ. With some algebra, we find

$$\sigma\left[\frac{\partial\zeta}{\partial x}\right]_{x=1} = -\left[\frac{\partial\zeta}{\partial x}\right]_{x=\delta_M}, \tag{46}$$

and

$$\left[\frac{\delta_M}{\alpha}(1+\sigma-\alpha)+1\right]\sigma\left[\frac{\partial\zeta}{\partial x}\right]_{x=1} = (1+\sigma)\frac{\phi_p}{2} - [\zeta]_{x=1} - \sigma[\zeta]_{x=\delta_M}. \tag{47}$$

At the start of the charging process, $\zeta(x,0)=0$ and at its conclusion, $\zeta(x,\infty)=\phi_p/2$. The solution to (45), satisfying the conditions (46) and (47), is

$$\frac{\zeta(x,t)}{\phi_p/2} = 1 - \sum_{n=1}^{\infty} A_n\, e^{-\frac{\sigma\lambda_n^2}{1+\sigma}t}\big(\sigma\cos(\lambda_n(1-x)) + \cos(\lambda_n(x-\delta_M))\big). \tag{48}$$

In the above,

$$A_n = \frac{2}{\lambda_n}\frac{(1+\sigma)\sin\big(\lambda_n(1-\delta_M)\big)}{\big[1+\sigma^2+2\sigma\cos\big(\lambda_n(1-\delta_M)\big)\big](1-\delta_M) + \left[\frac{\delta_M}{\alpha}(1+\sigma-\alpha)+1\right]\sigma\sin^2\big(\lambda_n(1-\delta_M)\big)}. \tag{49}$$

The eigenvalues λ_n are the roots of the equation

$$2\sigma + (1+\sigma^2)\cos\big(\lambda_n(1-\delta_M)\big) = \left[\frac{\delta_M}{\alpha}(1+\sigma-\alpha)+1\right]\sigma\lambda_n\sin\big(\lambda_n(1-\delta_M)\big). \tag{50}$$

Witness that when $\sigma=1$ and $\lambda_n(1-\delta_M)=n\pi$ ($n=1,3,5,\ldots$), both sides of equation (50) are equal to zero. The corresponding $A_n \equiv 0$ (49) and these spurious eigenvalues do not contribute to the series.

Integrating (48) over half of the cell ($\delta_M \le x \le 1$), we find the charge accumulation

$$q(t) \approx q_\infty - \frac{\phi_p}{2}\sum_{n=1}^{\infty}\frac{A_n}{\lambda_n}(1+\sigma)\sin\big(\lambda_n(1-\delta_M)\big)e^{-\frac{\sigma\lambda_n^2}{1+\sigma}t} \tag{51}$$

as a function of time. In the limiting case when the solid matrix has an infinite conductivity ($\sigma\to\infty$), expressions (48), (50) and (51) reduce to the corresponding expressions derived in the previous section.

As in the previous section, we use the leading eigenvalue λ_1 to estimate the system's characteristic charging time $t_{1/2}$. In the limit of low matrix conductivity ($\sigma\to 0$), the leading eigenvalue

$$\lambda_1 \sim \frac{1}{1-\delta_M}\frac{\pi}{2}\left[1+\left(\frac{4}{\pi}-1-\frac{1}{\beta}\right)\sigma+O(\sigma^2)\right]. \quad (52)$$

The corresponding characteristic charging time is

$$t_{1/2}^{\sigma\to 0} \sim 0.196(1-\delta_M)^2\left[\frac{1}{\sigma}+\left(1.39+\frac{4.07}{\beta}\right)+O(\sigma)\right]. \quad (53)$$

The asymptotic limit for the large matrix conductivity $t_{1/2}^{\sigma=\infty}$ was derived in the previous section. Combining $t_{1/2}^{\sigma\to 0}$ with the charging time $t_{1/2}^{\sigma=\infty}$ for systems of infinite conductive solid matrix (equation 41 or 42), we construct a composite charging time

$$t_{1/2}^{comp} \sim 0.196\frac{(1-\delta_M)^2}{\sigma}+t_{1/2}^{\sigma=\infty}. \quad (54)$$

In the case of the solid matrix with infinite conductivity, the charging process is controlled by the pore and separator resistances to ion transport. When the matrix has finite conductivity, there is an additional resistance - the electrical resistance of the solid matrix to electron flow that scales like $(1-\delta_M)/\sigma$. Hence, when the solid matrix resistance dominates, the charging time $t_{1/2}\sim q_\infty\,(1-\delta_M)/(\sigma\phi_p)$, which is consistent with the prediction of equation (53).

We solved the full nonlinear equations (10-12) with COMSOL™. When implementing the boundary condition (14), we used a COMSOL build-in, smoothed step function to ramp up the applied potential difference over a short time interval to approximate the Heaviside step function while avoiding the non-physical oscillations resulting from the Gibbs phenomenon. Fig. 8 depicts the spatial distributions of the zeta potential $\zeta(x,t)$ at various times for two values of the solid matrix conductivities, $\sigma=1$ (a) and $\sigma=0.01$ (b), and compares the analytical solution (48) (solid lines) with the finite element one (hollow circles). When $\sigma=1$ (Fig. 8a), the series (48) converges rapidly, requiring only 15 terms to achieve sufficient precision. The finite element solutions are in excellent agreement with the analytical ones. At early times, ζ deviates from zero close to both the current collector ($x=1$) and the separator surface ($x=\delta_M$, gray bar), indicating that the charging process starts at both ends of the porous matrix. This should be contrasted with the case of the solid matrix with infinite conductivity, where the charging starts only next to the separator's interface. As time increases, so does the zeta potential until it eventually attains the uniform value of $\phi_p/2$, once the EDL has been fully established.

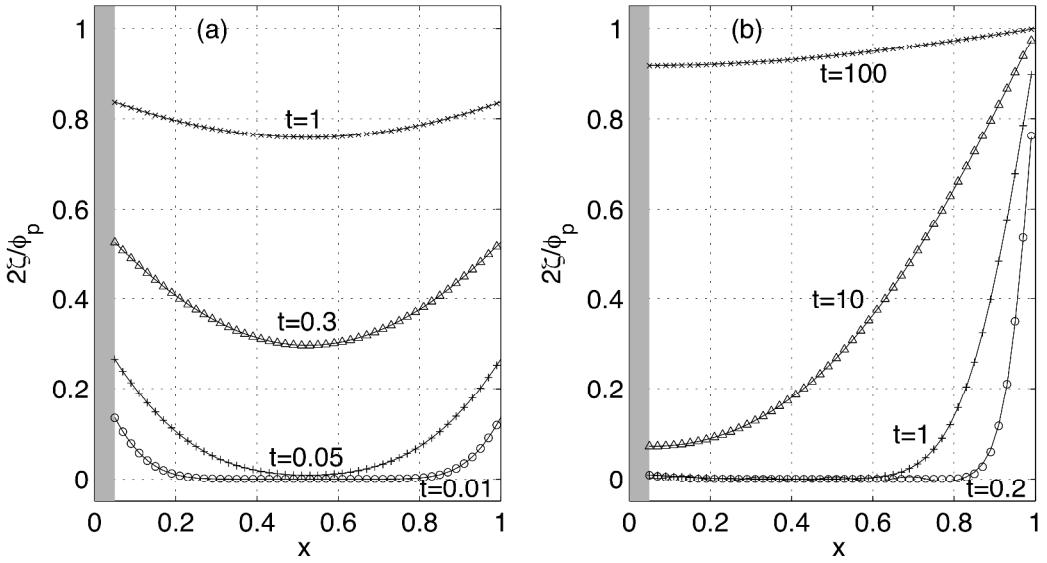

Figure 8: The normalized zeta potential $\zeta = \phi_m - \phi_e$ as a function of position at various times when (a) $\sigma = 1$, $t = 0.01(\odot)$, $0.05(+)$, $0.3(\Delta)$, $1(\times)$; and (b) $\sigma = 0.01$, $t = 0.2(\odot)$, $1(+)$, $10(\Delta)$, $100(\times)$. Solid lines and symbols correspond, respectively, to the analytical and finite element solutions. $\phi_p = 0.4$, $\delta_p = 0.005$, $\delta_M = 0.05$, $\alpha = 1$.

When $\sigma = 0.01$ (Fig. 8b) and at short times, the series (48) converges slowly, requiring about 50 terms to achieve sufficient precision. Witness that at early times, the zeta potential exhibits a steep boundary layer of thickness $O(\sigma)$ next to the current collector ($x = 1$). Due to the slow electron flow in the solid matrix, initially the charging process takes place only at the current collector and not next to the separator. Thus, at short times, it would be more appropriate to approximate the medium as semi-infinite, instead of using the series solution.

Fig. 9a depicts the normalized stored charge $q(t)/q_\infty$ as functions of time. When $\sigma \geq 10$, the charging process is nearly identical to the case of a solid matrix with infinite conductivity, and $t_{1/2}^{\sigma=\infty} \sim 0.2$. Fig. 9b depicts the computed charging time $t_{1/2}$ (symbols), the prediction for small σ (53, solid line) and the composite estimate (54, dashed line) as functions of the solid matrix conductivity (σ). Witness the excellent agreement between the finite element results and the estimate (53) when $\sigma \leq 1$. When $\sigma > 1$, the estimate (53) starts to deviate from the finite element solution. Overall, the composite solution (54) fits well with the finite element solution over the whole range of matrix conductivities. It should be noted that the steady state ion concentrtion c_∞

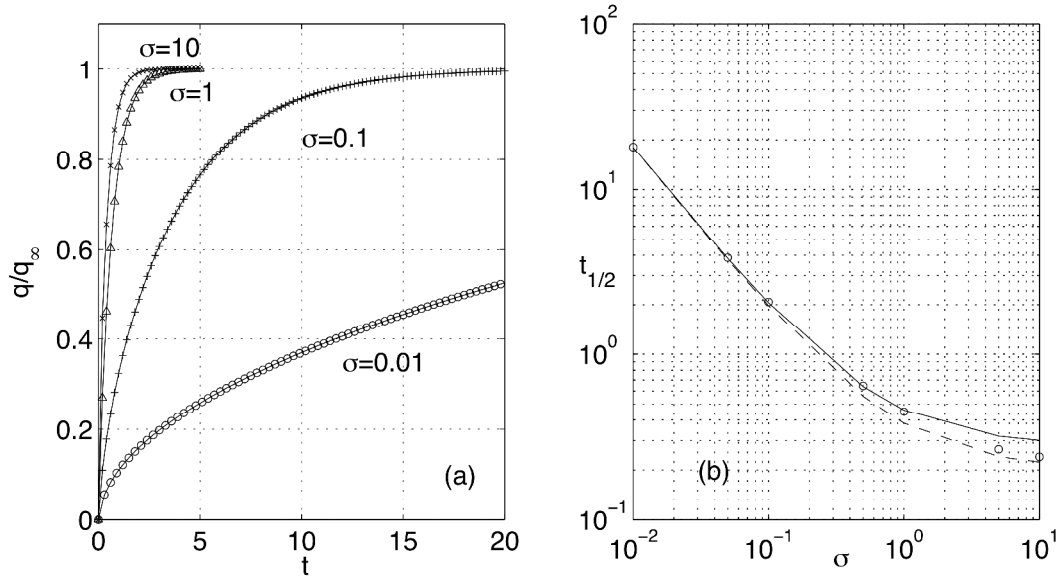

Figure 9: (a) The accumulated charge $q(t)/q_\infty$ as a function of time when σ =0.01(⊙), 0.1(+), 1(△), and 10(×); and (b) the charging characteristic time $t_{1/2}$ as a function of solid matrix conductivity. The solid line, dashed line, and hollow circles correspond, respectively, to the theoretical prediction (53), the composite estimate (54), and the finite element solution. $\phi_p = 0.4, \delta_p = 0.005$, $\delta_M = 0.05$, and α =1.

and the total accumulated charge q_∞ are still, respectively, given by equations (26) and (27), independent of the electrolyte diffusivity and the solid matrix conductivity.

Next, we consider the case of a relatively large potential $\phi_p = 40$ and a finite solid matrix conductivity $\sigma = 0.1$. Fig. 10 depicts the normalized zeta potential (a) and the electrolyte concentration (b) as functions of the spatial position at various times. At $t = 0$, there is no EDL and $\zeta = 0$. During the charging process, the zeta potential increases until it achieves its long time asymptotic value of $\phi_p/2$. As in the case of the small potential (Fig. 8), the zeta potential first increases (mostly) next to the current collector and next to the separator, and then, as time increases, the fronts diffuse into the half cell's interior. As the EDL charges up, the electrolyte concentration decreases from unity to the steady state equilibrium value c_∞ (equation 26). In contrast to the case of the highly conductive matrix (Fig. 4b), where the charging process started next to the separator ($x = \delta_M$), in the low conductivity case, most of the charging first occurs next to the current collector ($x = 1$). This is because, in the low conductivity limit, the process is limited by the electron flow through the solid matrix while in the high conductivity case the process is controlled by ion transport.

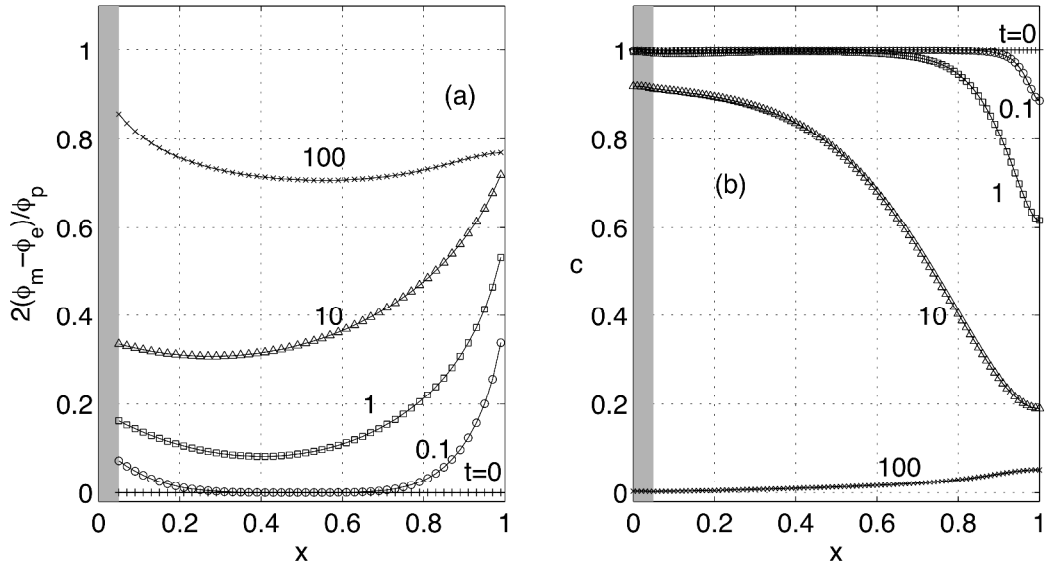

Figure 10: The normalized zeta potential ζ (a) and the electrolyte concentration c (b) as functions of position x at various times: $t = 0$(+), 0.1(⊙), 1(□), 10(△) and 100(×). $\phi_p = 40$, $\delta_p = 0.005$, $\delta_M = 0.05$, $\alpha = 0.5$, and $\sigma = 0.1$.

Fig. 11a depicts the normalized, stored charge as a function of time for various solid matrix conductivities when $\phi_p = 40$. The charge accumulation curves approach the equilibrium value monotonically. When collecting plate potential was small (Fig. 9a), the approach to steady state was exponential and dominated by the leading eigenvalue (51). At large potentials, the approach to equilibrium is more complicated. Interestingly, when $\sigma = 1$, the charging process is more rapid than when $\sigma = 10$. Counter to intuition, $t_{1/2}$ does not necessarily decrease as the solid matrix conductivity increases.

Fig. 11b depicts the characteristic charging time $t_{1/2}$ as a function of the solid matrix conductivity for various applied potentials: $\phi_p = 10$, 20, 30 and 40. When $\phi_p = 10$, $t_{1/2}$ decreases monotonically as the matrix conductivity increases, similar to the small potential behaviour, and as $\sigma \to 0$, $t_{1/2} \sim \sigma^{-1}$. However, at larger potentials, the variation of the charging time is more complicated. As $\sigma \to 0$, the slope varies nonlinearly like $t_{1/2} \sim \sigma^{-k}$ where $0.5 < k < 1$, and k decreases as ϕ_p increases. When $\phi_p \leq 30$, the charging time $t_{1/2}$ decreases as σ increases, consistent with the intuition that reductions in the matrix resistance to electron transfer should speed up the charging process. When $\phi_p = 40$, counter to intuition, $t_{1/2}$ attains a

minimum at $\sigma\sim2.0$ and increases slightly when $\sigma > 2$. In other words, there is an optimal solid matrix conductivity at which the charging is the fastest. The conductivity that minimizes the charging time is a function of the applied potential ϕ_p. To better understand why there is a minimum in $t_{1/2}$, Fig. 12 depicts the concentration distributions at various instances during the charging process when the matrix conductivity is nearly optimal ($\sigma = 2$) (a) and when $\sigma = 10$ (b). When $\sigma = 10$, the ions in the pore electrolyte next to the separator are severely depleted, which blocks the ions' flux and slows down the charging process of the EDLs. When the matrix conductivity is optimal, the electric potential in the matrix (and the zeta potential) in the region next to the separator rise more gradually due to the slower flow of current in the solid matrix. Thus the ion depletion next to the separator is less severe than in Fig. 12b, resulting in an overall speed-up of the charging process. Since it is unlikely that one would be able to maintain high solid matrix conductivity in the EFC, it is reassuring that there is no severe loss of performance as long as the solid matrix conductivity is of comparable magnitude to that of the electrolyte ($\sigma \geq 1$). Furthermore, for large potentials, one may explore an optimal solid matrix conductivity that balances the electron flow into the solid matrix with the ion transport in the electrolyte to alleviate the severe ion depletion next to the separator.

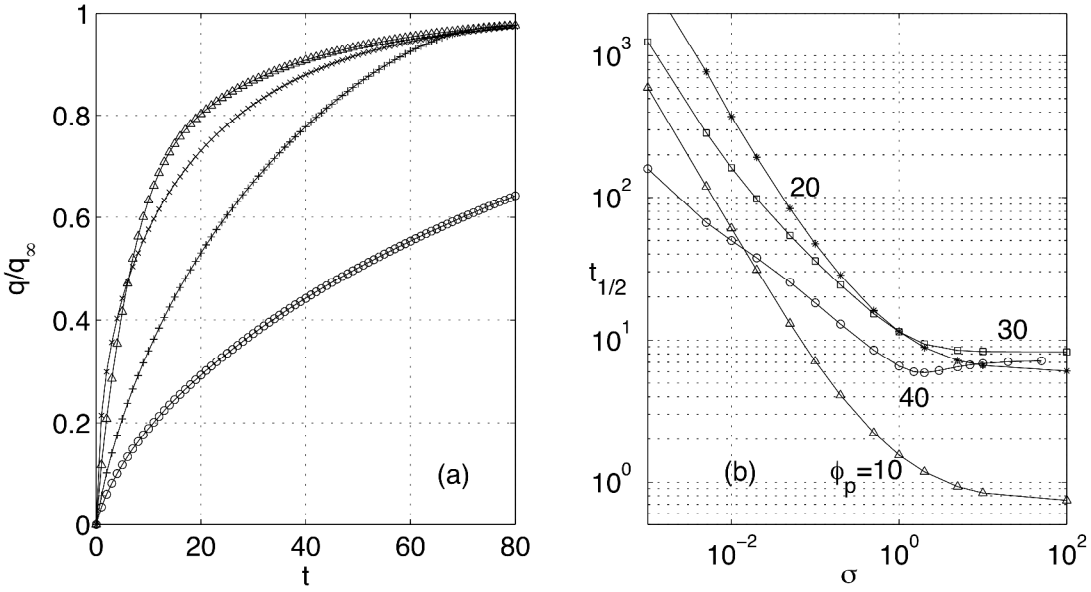

Figure 11: (a) The normalized stored charge $q(t)/q_\infty$ as functions of time for various matrix conductivities σ =0.01(⊙), 0.1(+), 1(△), and 10(×) when $\phi_p = 40$ and (b) the charging characteristic time $t_{1/2}$ as a function of solid matrix conductivity when $\phi_p = 10$(△), $\phi_p = 20$(∗), $\phi_p = 30$(□), and $\phi_p = 40$(⊙). $\delta_p = 0.005$, $\delta_M = 0.05$, and α =1.

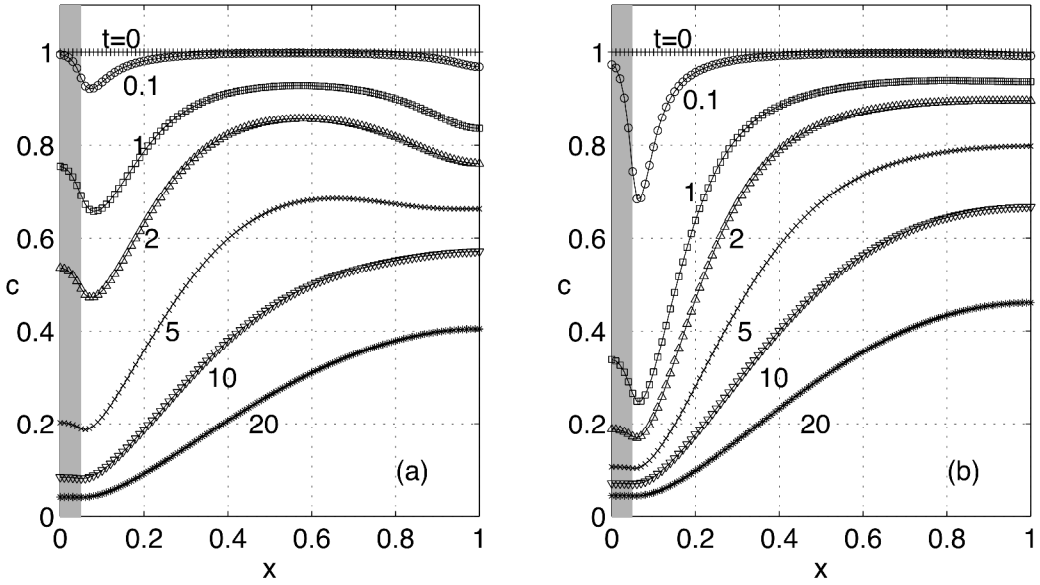

Figure 12: The electrolyte concentrations c as functions of position at various times when σ=2 (a) and σ=10 (b): $t = 0(+)$, $0.1(\odot)$, $1(\square)$, $2(\triangle)$, $5(\times)$, $10(\nabla)$ and $20(*)$. $\phi_p = 40$, $\delta_p = 0.005$, $\delta_M = 0.05$, $\alpha = 1$.

3 Conclusions

In this study, we considered the charging dynamics of an EFC cell subjected to a step change in the collecting plates' potential when the porous electrodes are ideally polarizable, the electric double layer is thin, and the electrolyte is dilute, symmetric, and binary. We have formulated a mathematical model based on the volume averaging (homogenization) theory for porous electrodes and modeled the electric double layer with the classical Gouy-Chapman-Stern model. We have examined both the case of a solid matrix with infinite electric conductivity and the case of a solid matrix with finite electric conductivity. For each of the cases, we derived closed form solutions for small potential. These analytical solutions provided insights into the physics of the problem and provided partial verification of numerical solutions. For relatively large collecting plate potentials, we solved the mathematical model numerically with finite elements. The analysis of the infinite conductivity case augments and supplements results previously presented in Biesheuvel and Bazant [17]. The finite conductivity case is new and was analyzed here for the first time.

For the case of the EFC cell with infinite matrix conductivity, we have identified two mechanisms that control the charging process: the ions' flux across the insulating spacer and the ions' flux in the bulk of the cell. Based on these mechanisms, we derived closed form expressions to estimate the characteristic charging time.

In the case of the EFC cell with finite matrix conductivity, the rate of current flow through the solid matrix also controls the charging process. Significantly, our calculations demonstrate that there is no significant deterioration in performance when a finite conductivity matrix is used as long as the matrix conductivity is not lower than that of the electrolyte solution ($\sigma \geq 1$). Furthermore, when the applied potential is relatively large, there is an optimal matrix conductivity that minimizes the charging time. At this optimal matrix conductivity, the electron flow into the solid matrix balances with the ion transport in the electrolyte to alleviate the severe ion depletion next to the separator, resulting in an overall speed-up of the charging process.

Acknowledgments

The work was supported, in part, by the State of Pennsylvania's Ben Franklin Technology Development Authority - the Energy Commercialization Institute (ECI).

References:

1. Electrical Energy Storage Technology Options, Report 1020676, Electric Power Institute, Palo Alto, CA 2010. Also "Energy Storage for the Electric Grid: Benefits and Market Potential Assessment, Report SAND 2010-0815, Sandia National Laboratories, Albuquerque, NM, 2010.
2. EPRI-DOE Handbook of Energy Storage for Transmission and Distribution Applications, 1001834, EPRI, Palo Alto, CA and the US DOE, Washington DC. (2003)
3. Dunn, B., Kamath, H., and Tarascon, J-M, Electrical Energy Storage for the Grid: A battery of choices, *Science* **334**, 928. (2011)
4. Risser, S., Beach, E., Moore, M., and Koper, O., Application of Metal Oxide Supercapacitors for Naval Applications, (2012) https://www.navalengineers.org/ProceedingsDocs/ASNE%20Day%202012/Papers/Risser.pdf
5. E. Faggioli, P. Rena, V. Danel, X Andrieu, R. Mallant, H. Kahlen, Supercapacitors for the energy management of electric vehicles, *J. Power Sources* **84**, 261-269. (1999)
6. Conway, B., E., Electrochemical Supercapacitors: Scientific Fundamentals and Technological Applications, Kluwer Academic/Plenum Publishers, New York. (1999)

7. http://batteryuniversity.com/learn/article/whats_the_role_of_the_supercapacitor
8. D. H. Doughty, P.C. Butler, A.A. Akhil, N.H. Clark, and J.D. Boyes, Batteries for Large-Scale Stationary Electrical Energy Storage, *Electrochemical Society Interface* **19** (3), 49. (2010)
9. T. Nguyen and R. F. Savinell, Flow Batteries, *Electrochemical Society Interface* **19** (3), 54. (2010)
10. Chian Y., M, Carter W., C, Ho, B., Y, Duduta, M., Int. Patent Application WO2009151639A1. (2009)
11. Duduta, M., Ho, B., Wood, V., C., Limthongkul, P., Brunini, V., E., Carter, W., C., and Chiang, Y-M, Semi-Solid Lithium Rechargeable Flow Battery, *Advanced Energy Materials* **1**, 511-516. (2011)
12. Brunini, V., E., Chiang, Y-M, and Carter, W., C., Modeling of Hydrodynamic and Electrochemical Efficiency of Semi-Solid Flow Batteries, *Electrochimica Acta* **69**, 301-307. (2012)
13. Presser, V., Dennison, C., R., Campos, J., Knehr, K., Kumbur, E., C., and Gogotsi, Y., The Electrochemical Flow Capacitor: A New Concept for rapid Energy Storage and Recovery, *Advanced Energy Materials* **2** (7), 895-902. (2012)
14. Kastening, B., Boinowitz, T., and Heins, M., Design of slurry electrode reactor system, *J. Applied Electrochemistry* **27**, 147-152. (1997)
15. Gouy, M., Sur la constitution de la charge électrique à la surface d'un électrolyte, *J. Phys. Theor. Appl.* **9**, 457-467. (1910)
16. Chapman, D. L., A contribution to the theory of electrocapillarity, *Philosophical Magazine* **25**, 475-481. (1913)
17. Biesheuvel, P. M. and Bazant, M. Z., Nonlinear dynamics of capacitive charging and desalination by porous electrodes, *Physical Review E* **81**, 031502. (2010).
18. Newman, J., and Tiedemann, W., Porous-Electrodes Theory with Battery Applications, *AIChE J.* **21** (1), 25-41, (1975).
19. Yan, X., Wang, Q., and Bau, H., H., Dispersion in Retentive Pillar Array Columns, *J. Chromatography A* **1217**, 1332–1342. (2010)
20. Newman, J., and Thomas-Alyea, K., E., *Electrochemical Systems*, Wiley-Interscience, Englewood Cliffs, NJ, pp 186-208. (2004)
21. Kilic, M. S., Bazant, M. Z., Ajdari, A., Steric effects in the dynamics of electrolytes at large applied voltages. I. Double-layer charging, *Physical Review E* ***75***, 021502. (2007)
22. Kilic, M. S., Bazant, M. Z., Ajdari, A., Steric effects in the dynamics of electrolytes at large applied voltages. II. Modified Poisson-Nernst-Planck equations, *Physical Review E* ***75***, 021503. (2007)
23. Oren Y., Capacitive deionization (CDI) for desalination and water treatment – past, present and future (a review), *Desalination* **228**, 10–29 (2008).
24. Porada, S., Zhao, R., van der Wal, A., Presser, V., Biesheuvel, P.M., Review on the science and technology of water desalination by capacitive deionization, *Progress in Materials Sci.* **58**,1388–1442. (2013)

25. Jeon, S-I, Park, H-R, Yeo, J-G, Yang, S, Cho, C.H, Han, M.H, Kim, D. K., Desalination via a new membrane capacitive deionization process utilizing flow electrodes. *Energy Environ Sci.* **6**, 1471-1475. (2013).
26. Newman, J.S., and Tobias, C.W., Theoretical analysis of current distribution in porous electrodes, *J. Electrochem. Soc.* **109**, 1183-1191, (1962).
27. Johnson, A.M., and Newman, J., Desalting by means of porous carbon electrodes, *J. Electrochem. Soc.* **118**, 510-517, (1971).
28. Biesheuvel, P.M., Fu, Y., Bazant, M.Z., Diffuse charge and Faradaic reactions in porous electrodes, *Physical Review E* **83**, 061507. (2011).
29. Zhao, R., van Soestbergen, M., Rijnaarts, H.H.M., van der Wal, A., Bazant, M.Z., Biesheuvel, P.M., Time-dependent ion selectivity in capacitive charging of porous electrodes, *J. Colloid Inter. Sci*. **384**, 38-44 (2012)
30. Rica R.A., Ziano, R., Salerno, D., Mantegazza, F., Bazant, M.Z., Brogioli, D., Electro-diffusion of ions in porous electrodes for capacitive extraction of renewable energy from salinity differences, *Electrochimica Acta* **92**, 304-314 (2013).
31. Hatzell, K. B., Iwama, E., Ferris, A., Daffos, B., Urita, K., Tzedakis, T., Chauvet, F., Taberna, P., Gogotsi, Y., Simon, P., Capacitive deionization concept based on suspension electrodes without ion exchange membranes, *Electrochemistry Comm.* **43**,18–21 (2014).
32. Mirzadeh, M., Gibou, F., Squires, T. M., Enhanced charging kinetics of porous electrodes: surface conduction as a short-circuit mechanism, *Phys. Rev. Lett.* **113**, 097701 (2014).
33. Jeon, S-I, Yeo, J-G, Yang, S, Choi, J., Kim, D. K., Ion storage and energy recovery of a flow-electrode capacitive deionization process. *J. Mater. Chem. A* **2**, 6378-6383. (2014).
34. Porada, S., Weingarth, D., Hamelers, H. V. M., Bryjak, M., Presser, V., and Biesheuvel, P. M., Carbon flow electrodes for continuous operation of capacitive deionization and capacitive mixing energy generation, *J. Mater. Chem. A* **2**, 9313-9321. (2014)